Development of scalable deconvolution methods for determining secondary target neutron yields from dual-thick-target cosmic-ray ion accelerator experiments

Hunter N. Ratliff[a,b,*], Natalie A. McGirl[a], Matthew R. Beach[c], Luis A. Castellanos[a], Martha S. Clowdsley[d], Lawrence H. Heilbronn[a], Chiara LaTessa[e,f], John W. Norbury[d], Adam Rusek[g], Michael Sivertz[g], Ashwin P. Srikrishna[a], Hui-Chen Wang[a], Cary Zeitlin[h]

[a]*Nuclear Engineering Department, University of Tennessee, 1412 Circle Dr., Knoxville, TN 37916, USA*
[b]*Japan Atomic Energy Agency, 2-4 Shirakata, Tokai, Naka, Ibaraki 319-1195, Japan*
[c]*National Institute of Aerospace, 100 Exploration Way, Hampton, VA 23666, USA*
[d]*National Aeronautics and Space Administration Langley Research Center, Hampton, VA 23681-2199, USA*
[e]*University of Trento, Via Calepina, 14-38122 Trento TN, Italy*
[f]*TIFPA - INFN, Via Sommarive, 14-38123 Povo, Trento TN, Italy*
[g]*Brookhaven National Laboratory, PO Box 5000, Upton, NY, 11973-5000, USA*
[h]*Leidos, Inc., 2625 Bay Area Blvd., Houston, TX 77058, USA*

Abstract

Recent experiments emulating the deep-space radiation environment within an enclosed spacecraft were conducted at the NASA Space Radiation Laboratory; this was achieved by bombarding various combinations of two consecutive thick targets with Galactic Cosmic Ray-like particle beams. While all secondary particles generated in the first of these two targets could be characterized using time-of-flight techniques, characterization of the neutrons produced in the second target, emulating the "back wall" of a spacecraft, required the development and implementation of deconvolution techniques. This work covers this methodology, its validation, and the systematic results present within this benchmark dataset of neutron yields from the secondary target.

Keywords: neutron, space radiation, shielding, benchmark, deconvolution, Tikhonov regularization

1. Introduction

Mitigating the risk posed by the radiation environment in space is one of the key challenges which must be addressed for future crewed missions to Mars and other long-term deep-space objectives to be viable. The accelerator-based experiment featured in this work assembled a benchmark dataset of secondary particle yields as a representative set of those generated from the interactions of galactic cosmic rays (GCRs) with the walls of a spacecraft. Unique to this experiment was the inclusion of a secondary thick target located downstream of the primary thick target, allowing for accurate representation of the neutrons produced from the interactions of all particles (penetrating primary particles and their secondary particles generated in the first wall) passing through the second wall of the enclosed environment of a spacecraft.

The experiments were motivated by earlier NASA work involving simulations of a thin water slab sandwiched between two shielding slabs bombarded by GCRs; the study showed that, for aluminum shielding, there was an optimal thickness around 20 g/cm² which minimized astronaut dose equivalent, as shown in Figure 1 [1]. Beyond this optimal thickness, most of the rise (~70%) in dose equivalent

in the simulated water slab was found to be attributable to protons which were primarily (~75%) produced from neutron interactions [1].

As indicated by the straight-ahead only (N=1), bidirectional (N=2, straight-ahead plus backscatter), and 3D approximation (N=34) calculations with the deterministic 3DHZETRN code shown in Figure 1, neutrons traveling from the second wall back to the water slab were responsible for this build-up in dose equivalent. While no such optimal thickness was found for polyethylene shielding, it is evident that additional shielding beyond 20–30 g/cm² of polyethylene yields little benefit, signaling the possibility of a financially optimal thickness.

At the energies of the GCR ions, fragmentation reactions typically result from their collision with any other nuclei. Past studies have shown that there are discrepancies in the fragmentation cross sections between experimental data and the various particle transport codes useful for modeling these space environments [2]. These discrepancies propagate through simulations modeling realistic shields (in materials and thicknesses) and can result in sometimes stark differences, particularly in the production of neutrons and complex light ions [1, 3].

To further investigate results from past studies, the experiment was designed to generate a benchmark dataset which specifically focused on studying the neutrons and

---

*Corresponding author.
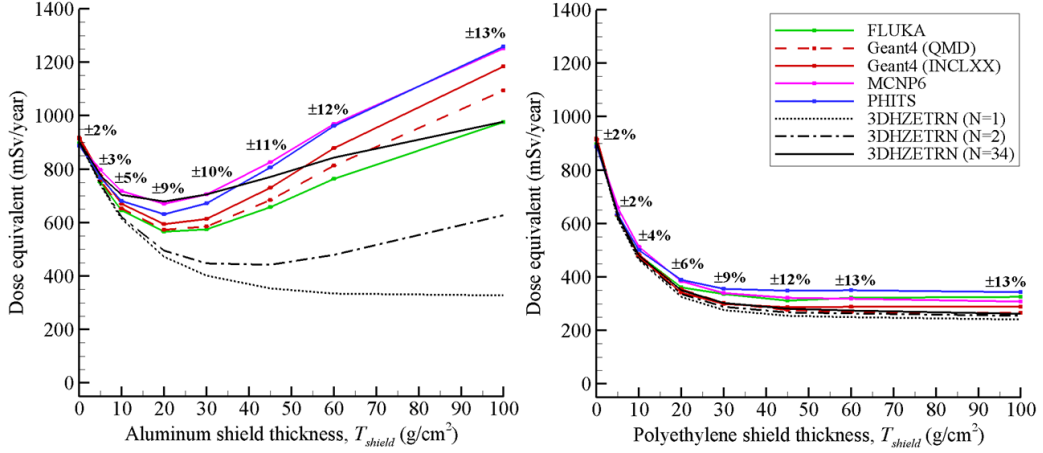Email address:* `hratliff@vols.utk.edu` (H. N. Ratliff)

Figure 1: Simulated dose equivalent inside of a water slab sandwiched between two slabs of varying thicknesses of aluminum or polyethylene being bombarded by GCRs; figure from Reference 1.

complex light ions produced in these interactions of GCRs with spacecraft materials. This paper specifically focuses on detailing the methods used to characterize the neutrons produced in the secondary downstream target, proving the validity and performance of those methods, and showcasing the systematic trends present in those results. The neutrons produced in the primary upstream target are discussed in detail in Reference 4.

2. Experiment

The experimental design is summarized in detail in Reference 5. In short, fifteen GCR-like beams consisting of five species (^{1}H, ^{4}He, ^{12}C, ^{28}Si, and ^{56}Fe) each at three energies (400 MeV/n, 800 MeV/n, and either 2500 MeV for H or 1500 MeV/n for $Z > 1$ beams) were accelerated into eight dual-target configurations emulating spacecraft shielding, listed in Table 1. Neutrons and light ions were detected in six organic liquid scintillator (OLS) detectors placed at 10°, 30°, 45°, 60°, 80°, and 135° with respect to the center of the primary (upstream) target and the beamline. A schematic of the floor plan is shown in Figure 2.

Table 1: Tested primary + secondary target configurations. Note that in configurations 7* and 8* the Al target portion was always placed upstream from the HDPE portion.

No.	Primary target	Secondary target
1	20 g/cm^2 Al	60 g/cm^2 Al
2	40 g/cm^2 Al	60 g/cm^2 Al
3	60 g/cm^2 Al	60 g/cm^2 Al
4	20 g/cm^2 HDPE	60 g/cm^2 HDPE
5	40 g/cm^2 HDPE	60 g/cm^2 HDPE
6	60 g/cm^2 HDPE	60 g/cm^2 HDPE
7*	10 g/cm^2 Al + 10 g/cm^2 HDPE	60 g/cm^2 HDPE
8*	10 g/cm^2 Al + 50 g/cm^2 HDPE	60 g/cm^2 HDPE

Neutral particle events were separated from charged particles using thin plastic veto detectors placed on the exterior of the OLS detectors, and neutrons were separated from photons using pulse shape discrimination techniques. Neutrons from the primary target were isolated from all other neutrons by performing a background subtraction utilizing measurements made where the direct line from the primary target to each detector was blocked or "shadowed" with a long iron rod or "shadow bar" of diameter equal to that of the OLS detectors. After normalization, the neutron yield from the primary target is found by subtracting the measurements with a shadow bar in place from those without. This required repeating every measurement with and without a shadow bar concealing each detector. The shadow bar blocks neutrons coming from the primary target that would otherwise enter the detector. To study the neutrons produced in the secondary target (and those scattered throughout the room and from true background), only the measurements made where each detector is shadowed are necessary.

3. Analysis and deconvolution methodologies

Secondary particles produced in the primary target were characterized with time-of-flight techniques because their flight paths were well-known. However, this is not the case for the neutrons detected when the shadow bars were in place and blocking neutrons from the primary target; therefore, time-of-flight techniques cannot be used here to accurately characterize the neutron energy spectra. Instead, neutron energy information must be generated on a statistical basis from the collected pulse height spectra in the scintillators. One implication of this is that neutrons produced in the secondary target cannot be distinguished from neutrons produced elsewhere which scatter into a detector or neutrons from the natural background. However, for the detectors located closest to the downstream secondary target, the neutrons produced in the secondary
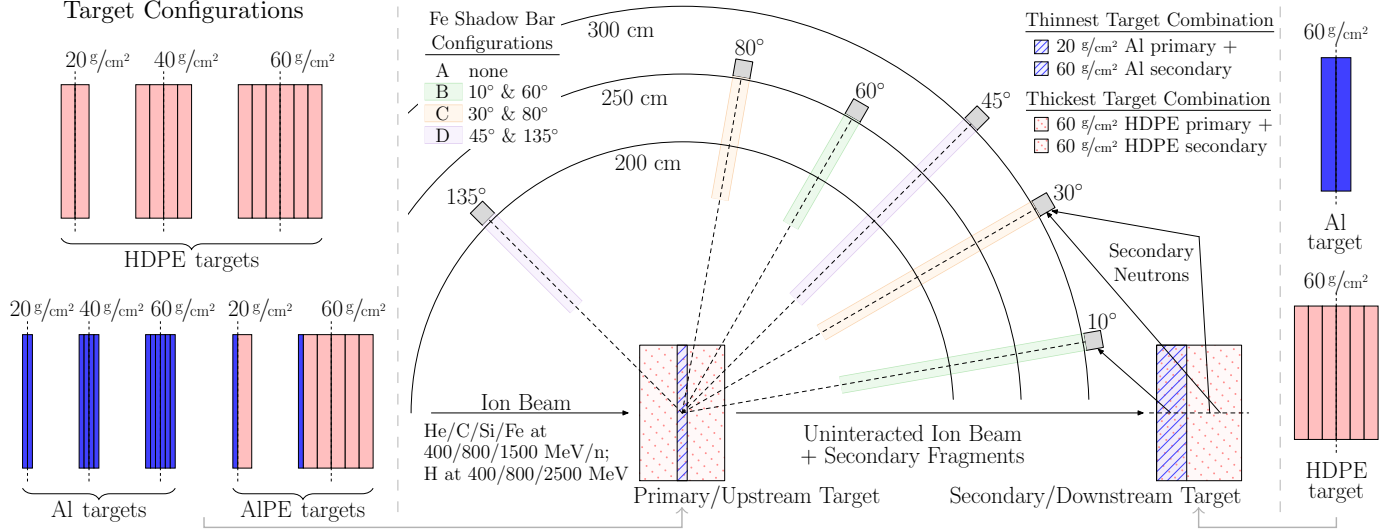
2

Figure 2: A to-scale schematic of the beam/detector/target system and the 8 primary and 2 secondary target configurations (mass centers indicated with dashed lines); the physically thinnest (hatched blue) and thickest (dotted red) targets are featured in the system drawing. Measurements were made in each of the 4 shadow bar configurations for all 120 ion beam and target configuration combinations.

target vastly outnumber those from elsewhere. This is due to the higher solid angle exposure and that the majority of fragments generated (along with any surviving primary beam ions) have very forward-peaked trajectories leading into the secondary target; this trend is also observed in the results as diminishing shadowed neutron count rates as a function of detector distance from the secondary target, an effect which would not be observed prominently if the room scattering neutron component was dominant.

Another consequence of not knowing the production point and flight paths of these neutrons is that their spectra can no longer be normalized to solid angle. Thus, the final spectra from the secondary downstream target reported in this work are single differential energy-dependent yield spectra. Spectra are normalized to energy bin width, the number of valid source beam particles striking the primary target, the live time of the detection system, and intrinsic detection efficiency.

The signal created from energy deposited by neutron interactions in the OLS is read out and digitized with a charge-to-digital converter (the term "pulse height" in this paper will refer to the amount of charge collected from the signal). Calibration measurements with ^{60}Co and ^{137}Cs photon sources were used to relate the measured raw digital values to pulse heights in units of MeV electron equivalent (MeVee). To extend the range of pulse heights that could be distinguished (and not fall into a lower or upper pileup channel), every charge signal was split into two branches: one which was passed through attenuators before digitization and one which was not. The maximum discernible pulse height of the unattenuated signal corresponded to channels toward the lower end of the attenuated signal, allowing the two to be stitched together after conversion to units of pulse height. With no attenuation, the 10° detector pulse height spectrum ranged from 1.9

MeVee to 29.6 MeVee, greatly limiting the range of neutron energies which could be distinguished through deconvolution. Inclusion of the attenuated signal allowed the spectrum to be extended to 122.4 MeVee. The range of sensitive pulse heights, the scintillation material, and operating voltages for each detector are listed in Table 2.

Table 2: Detector properties and pulse height spectra MeVee bounds.

Detector angle	Detector material	Voltage (V)	minimum MeVee	maximum MeVee
10°	EJ-301	1500	1.9	122.4
30°	EJ-301	1400	1.3	110.9
45°	EJ-301	1400	1.3	116.9
60°	EJ-309	1800	0.9	34.8
80°	EJ-309	1800	0.5	22.8
135°	EJ-309	1900	0.5	16.1

3.1. Objectives and general approach

In this work, neutron energy spectra were generated using the pulse height spectra from the 5" × 5" EJ-301/EJ-309 OLS. Due to the stochastic nature of the processes involved in the energy deposition and light production by neutron interactions in scintillators (primarily through collisions with protons and carbon nuclei), a monoenergetic neutron source will yield a distributed pulse height response. Relating a measured pulse height spectrum to an energy distribution requires use of an unfolding or deconvolution procedure. For deconvolution to be a viable approach, two primary challenges must be overcome: (1) generation of an accurate and physically representative detector response function (which translates between neutron energy and pulse height) and (2) development and

implementation of an unfolding technique which is scalable for the large dataset present in this work.

The light response of a detector to a neutron source of variable energies and intensities can be represented as the sum of the individual pulse height spectra of the monoenergetic constituents of the incident neutron spectrum weighted by the intensity of each neutron energy present. In equation form, the detector's characteristic light response function $\overline{\overline{R}}$ multiplied by the incident neutron spectrum $\vec{\Phi}$ should yield the measured pulse height distribution $\vec{L}$ as shown in Equation 1 [6].

$$\vec{L} = \overline{\overline{R}}\vec{\Phi} \tag{1}$$

Equation 1 can be rearranged to show the incident neutron spectrum in terms of the response function and pulse height spectrum (Equation 2).

$$\vec{\Phi} = \overline{\overline{R}}^{-1}\vec{L} \tag{2}$$

However, a simple inversion is not a viable approach for deconvolution here since the response function is not necessarily a square matrix and any small uncertainties in the matrix can impact the inversion significantly. Additionally, this makes the nontrivial assumption on the availability of an accurate detector response function covering the desired neutron energy range. Response function matrices are composed of numerous pulse height spectra produced by various known neutron energies, and they are generally constructed either with experimentally measured pulse height spectra or with computer simulated pulse height spectra. While experimental measurements directly reflect the complex physics from a neutron entering a detector to producing a pulse of light, the number of neutron energies sampled is often limited, resulting in a response matrix of lower resolution. In addition, for this experiment, response measurements for a detector of a specific size and material for neutrons are needed for energies well beyond the highly studied fission energies; these are quite difficult to obtain since truly monoenergetic high energy (>100 MeV) neutron sources do not exist. However, high-energy measurements with similar detectors using a quasi-monoenergetic source with a very prominent single neutron energy peak (but still with a spectrum of lower energy neutrons) have been made before [7]. Simulated response functions offer the advantage of producing pulse height spectra for as many monoenergetic source neutrons as is desired; however, the physics within the code must accurately reflect reality for the response functions to be accurate.

3.2. Response matrix formation

In this work, model-generated response functions were employed in order to obtain highly resolved response functions which allowed for greater flexibility later in the analysis. The Japan Atomic Energy Agency code SCINFUL-QMD was explicitly designed for modeling liquid scintillator response to neutrons of a wide range of energies (up to 3 GeV) [8]. SCINFUL-QMD builds upon the SCINFUL library and code which characterizes neutron response from 0.1 MeV up to 80 MeV [9]. Cross section data from the SCINFUL library is extrapolated to 150 MeV, beyond which the quantum molecular dynamics plus statistical decay model (QMD+SDM) is employed to model nuclear reactions; data from more recent works are also utilized in the code [7, 10, 11].

While SCINFUL-QMD is capable of producing pulse height spectra for 3 GeV neutrons, there is an experimental limit to the range of neutron energies that can be easily distinguished from one another that is determined by the physical size of the detectors and the maximum amount of energy that can be deposited by the most prominent reaction (collision with a proton). In the EJ-301 detectors, 12.7 cm of scintillation material will range out a 123.5 MeV proton (calculated with SRIM [12]). The longest possible chord in these detectors is 17.96 cm, which would stop a 150.4 MeV proton [12]. Though it is unlikely that a neutron would interact right at this edge and generate a 150 MeV proton with the precise angle to reach the opposite "corner" of the detector, it serves as a good bounding case. Thus, a response matrix capped at 150 MeV, shown in Figure 3, was used in this work.
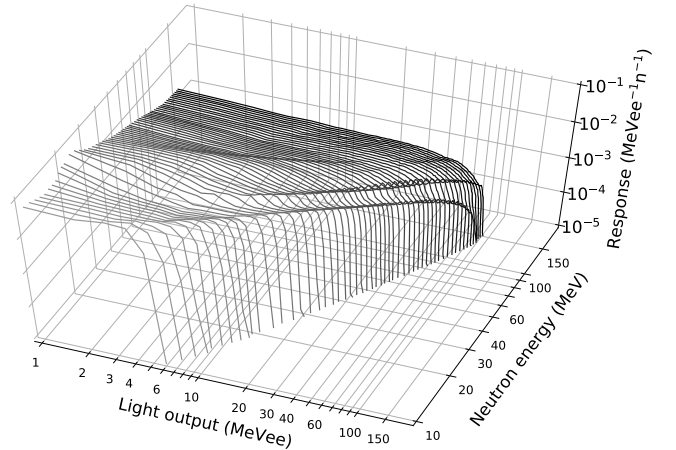

Figure 3: The response matrix from SCINFUL-QMD used before rebinning.

Around 120 MeV, the peak characteristic of the maximum recoil energy proton disappears, which makes sense given that only neutrons which enter from different angles or undergo numerous scattering reactions within the detector can possibly deposit more energy. Above this energy (especially beyond 150 MeV), the response matrix's individual pulse height spectra become increasingly difficult to distinguish from each other. Additionally, the maximum light output values of the response matrix illustrate that the usage of attenuated and unattenuated charge signals to extend the range of pulse heights detected was necessary to fully capture the signals produced by these neutrons, particularly in the three detectors closest to the secondary target.

3.3. Rebinning

For the deconvolution procedure to produce consistent results, the individual bins of each pulse height spectrum must contain a statistically significant amount of counts. For this analysis, an algorithm was written to process the 720 collected spectra, rebinning each spectrum to ideally contain at least 10 bins each of 5% or lower statistical uncertainty; this requirement was iteratively relaxed to produce a minimum of 5 bins each of 10% statistical uncertainty. The spectra for which this more relaxed criterion could not be achieved were deemed too statistically poor to be viable for deconvolution and were rejected. Of the 720 spectra, 200 were deemed not viable, but they were almost exclusively for the higher angled detectors and situations where statistics for all particles suffered due to limited beam currents available at NSRL. Only 5 of the 120 spectra for the 10° detector were deemed statistically insufficient.

This rebinning procedure resulted in spectra with a wide variety of binning structures. Since the deconvolution procedure is ultimately a series of matrix and vector operations, the pulse height axis of the response matrix must match that of the individual pulse height spectra to be deconvoluted. Thus, the response matrix's light axis was rebinned separately for each spectrum to be unfolded. Additionally, for the deconvolution to be valid and produce a unique result, the output quantity (neutron energy) must have a number of bins less than or equal to the number of input bins (pulse heights) [13]. This requirement necessitates rebinning of the energy axis of the custom response matrices with already rebinned light axes.

Making the response matrices square will simplify the deconvolution process; however, an important consideration must be made first. In cases where statistics were abundant and the rebinned pulse height spectrum still had many bins, attempting to match that same number of energy bins could result in oversampling the response function during the deconvolution process, producing an over-regularized solution. To prevent this, a limit of 10 evenly logarithmically-spaced neutron energy bins was imposed. In cases where the input spectrum had ten or fewer bins though, the energy axis was indeed rebinned to match that number and generate a square response matrix.

3.4. Deconvolution methodology

With the pulse height spectra and response matrices prepared, the next step is deconvolution. A step-by-step description of the deconvolution methodology is presented using downstream target-produced neutrons in the 10° detector from 800 MeV/n Fe projectiles incident on the 60 g/cm^2 HDPE upstream target followed by the 60 g/cm^2 HDPE downstream target as an example; the input pulse height spectrum for these neutrons is shown in Figure 4 ("s.p." stands for "source particle").

The matrix problem in Equation 1 can be solved using a non-negative least squares method (NNLS). The function
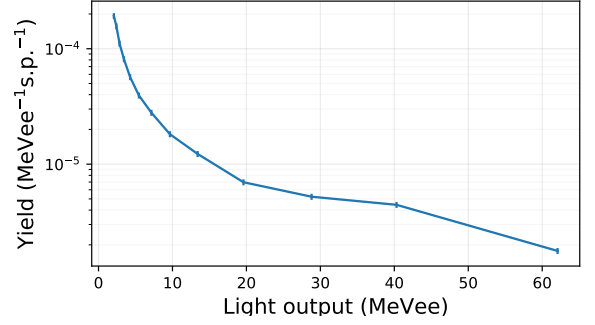

Figure 4: Input pulse height spectrum from 800 MeV/n Fe on HDPE at 10° (downstream target) (statistical uncertainty denoted by vertical error bars).

`scipy.optimize.nnls()` located in Python's SciPy optimization library was explicitly designed for this purpose and was utilized as an initial approach here; it simply requires the response matrix $\overline{\overline{R}}$ and a pulse height spectrum $\vec{L}$ and will output the incident neutron energy spectrum solution $\vec{\phi}$, solving Equation 3.

$$min_{\vec{\phi}} \left\| \overline{\overline{R}}\vec{\phi} - \vec{L} \right\|_2 \qquad (3)$$

The NNLS deconvoluted result using the input spectrum's tailor rebinned response matrix is shown in Figure 5; despite being the mathematically optimal solution, its jaggedness is clearly nonphysical, necessitating the development of a better approach.
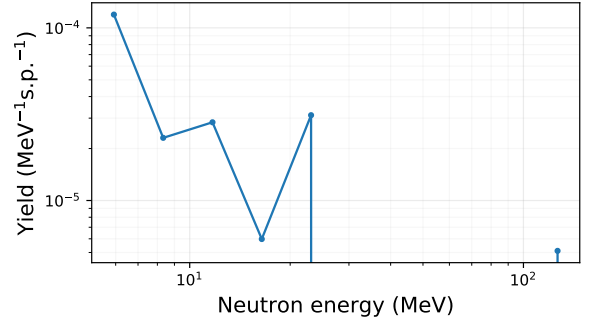

Figure 5: NNLS output spectrum from 800 MeV/n Fe on HDPE at 10° (downstream target). Points not plotted in frame are equal to zero.

Tikhonov regularization followed by L-curve analysis was employed in this research as that better approach. L-curve analysis is one of a variety of methods that can be used to determine an optimal level of regularization. A similar combination of Tikhonov regularization and L-curve analysis (among other tested methods) was successfully applied in a study on arms-control verification in Reference 6. Tikhonov regularization employs a regularization parameter μ whose "optimum" value is characterized by the elbow of the L-curve where a balance is struck between sacrificing the least amount of mathematical precision to

gain the most solution smoothness. This method is effectively solving Equation 4.

$$min_{\vec{\phi}} \left\| \overline{\overline{S}}_\mu \vec{\phi}_\mu - \vec{M} \right\|_2 \quad \text{where} \quad \overline{\overline{S}}_\mu = \begin{bmatrix} \overline{\overline{R}} \\ \mu \overline{\overline{1}} \end{bmatrix} \quad \text{and} \quad \vec{M} = \begin{bmatrix} \vec{L} \\ 0 \end{bmatrix}$$
(4)

Thus, to generate the L-curve (Figure 6), one must calculate the residual norm $||\overline{\overline{S}}_\mu \vec{\phi}_\mu - \vec{M}||_2$ and the solution norm $||\vec{\phi}_\mu||_2$ for a variety of values of μ. This work used approximately 30 values of μ to generate the L-curve for each spectrum.
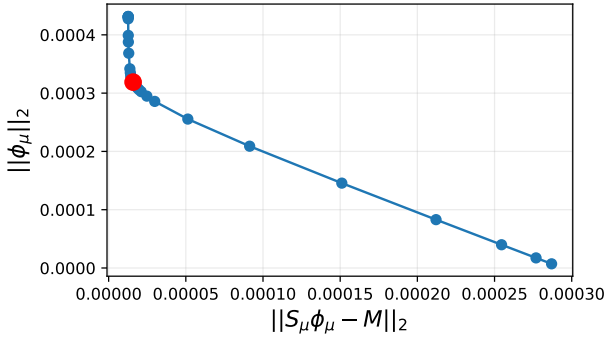
Figure 6: L-curve for the 800 MeV/n Fe on HDPE at 10° (downstream target) system. The elbow is denoted with a red dot.

As noted earlier, L-curve analysis is one of a variety of methods that can be used to identify a best regularization parameter. Historical applications of regularization often involved subjective selection of μ based on expectations of what the output spectrum should look like. However, with the scale of the dataset in this analysis and desire to minimize systematic uncertainties, such as those attributable to human judgment, a more robust and mathematically rigorous approach was used: L-curve analysis. For smaller datasets, the elbow point of the L-curve can be identified visually and correlated to a specific value of μ manually without much difficulty. However, in this analysis, the number of spectra make that approach overly cumbersome. Instead, an algorithmic and mathematically-based approach was employed: calculation of the curvature κ of the L-curve (Figure 7) as a function of the regularization parameter.

The curvature calculation (Equation 5, derived in Appendix A) is performed by fitting a circle to every three consecutive points on the L-curve, $(x_1, y_1), (x_2, y_2), (x_3, y_3)$, and taking the inverse of the radius of this circle.

$$\kappa = \frac{2 \cdot [((x_2 - x_1) \cdot (y_3 - y_2)) - ((y_2 - y_1) \cdot (x_3 - x_2))]}{\begin{array}{c} ([(x_2 - x_1)^2 + (y_2 - y_1)^2] \\ \cdot [(x_3 - x_2)^2 + (y_3 - y_2)^2] \\ \cdot [(x_1 - x_3)^2 + (y_1 - y_3)^2])^{1/2} \end{array}}$$
(5)

A "curvier" portion of a curve, such as an elbow-like bend, would be fit with a circle of smaller radius and thus higher curvature κ; therefore, the maximum value of the curvature corresponds to the value of μ closest to the elbow. By default, twenty values of μ ranging from 10^{-3} to 10^1 were used, but these ranges were expanded if the calculated L-curve elbow point was too close to either of the bounds. Once a rough value of μ had been determined, finer values of μ around the initial value were sampled to determine a more precise value of μ. A deeper explanation of Tikhonov regularization and the L-curve can be found in Reference 14 with a detailed look at the L-curve specifically in Reference 15.
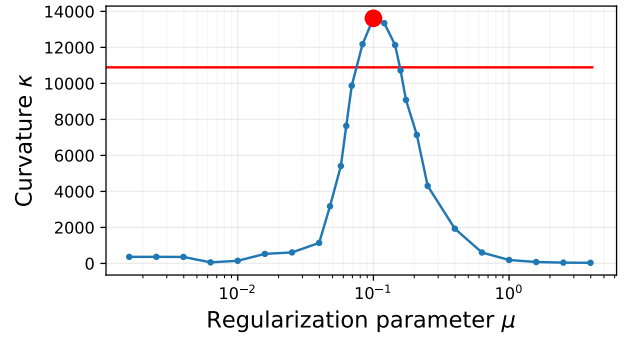

Figure 7: L-curve curvature κ (maximum denoted with a red dot and 80% of maximum denoted with a horizontal line).

In the example presented here, the spectrum shown in Figure 8 is the final output from the deconvolution with Tikhonov regularization. While still possessing some sharp features, it is continuous and considerably smoother than the NNLS result.
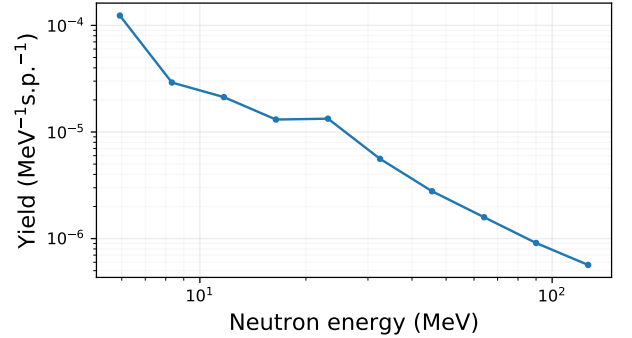

Figure 8: Tikhonov output neutron spectrum for the 800 MeV/n Fe on HDPE at 10° (downstream target) system.

3.5. Uncertainty quantification

Statistical uncertainties cannot be directly propagated from their initial pulse height spectra to the final yield spectra through the deconvolution process. Instead, a Monte Carlo approach to propagating the statistical uncertainties was employed here. Every bin in each pulse height spectrum had been rebinned to sufficient statistics

to claim that the counts in each bin were distributed normally around the average value with some standard deviation. To propagate these uncertainties, the deconvolution process for each input spectrum was repeated for a large number of trials (10, 000 in this work) where, rather than using the mean value of each pulse height spectrum data point, each data point was re-sampled using a normally distributed random number from the Gaussian distribution characteristic of that data point's mean value and standard deviation.

From the 10,000 resulting different energy spectra (all of identical energy bin structure) for each input pulse height spectrum, a new mean and standard deviation can be calculated for each final energy bin. Over many trials, the statistical uncertainties in each final spectrum will converge to some minimum value. Figure 9 shows the "exact" solutions from both the NNLS and Tikhonov-regularized approaches applied only once to the mean values of each input pulse height spectrum alongside the Monte Carlo (MC) averaged results with error bars denoting the statistical uncertainty propagated after 10,000 trials. The Tikhonov-regularized Monte Carlo result has converged and essentially overlaps with the initial solution. However, the NNLS results, while at least populating more energy bins over the ten thousand trials, still show sizable fluctuations, illustrating its high sensitivity to statistical fluctuations and further justifying the use of regularization.
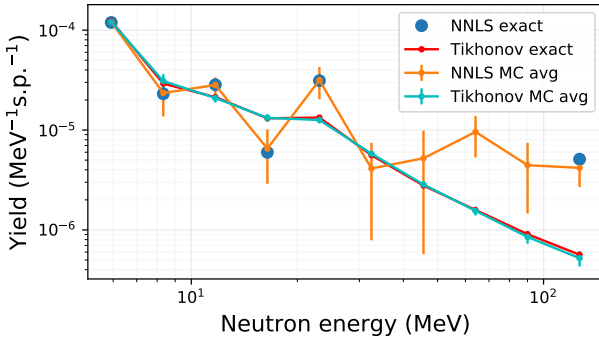

Figure 9: Monte Carlo averaged spectra results for the 800 MeV/n Fe on HDPE at 10° (downstream target) system.

In addition to statistical uncertainty, the final spectra also contain several sources of systematic uncertainty. A flat 10% uncertainty is assumed as a conservative estimate of the accuracy of the SCINFUL-QMD-generated response matrices and the code's ability to model detector response [8, 16, 17].

The choice of the specific regularization parameter μ and deviation from the "truest" solution from the NNLS calculation are not reflected in the statistical uncertainty calculation. A percent difference calculation of the Monte Carlo averaged Tikhonov-regularized (reference value) and NNLS spectra is used to account for the latter and is on average the primary driver of the total systematic uncer-

tainty. An uncertainty attributable to the specific choice of regularization parameter over its neighboring values resulting in similar curvatures κ on the L-curve was determined by taking the average of all spectra whose $\kappa(\mu)$ exceeded 80% of the maximum κ value and comparing that to the final spectrum produced with the optimal μ using a similar fractional error calculation. The horizontal line in Figure 7 denotes the 80% threshold.

The results are also subject to uncertainty attributable to any human judgment involved in the data analysis. This uncertainty is calculated by repeating all analysis steps involving human judgment and all subsequent analysis steps; afterward, the final spectra from the initial calculation and this second calculation undergo a percent difference calculation, yielding the systematic uncertainty attributable to that human judgment.

4. Results

The points within each spectrum are represented as shown in Figure 10 with a shaded box of arbitrary width and height which denotes statistical uncertainty and a cross whose vertical bar denotes total systematic uncertainty and horizontal bar denotes the energy bin width. The bin midpoint is taken to be the energy midpoint in $\log E$ space.
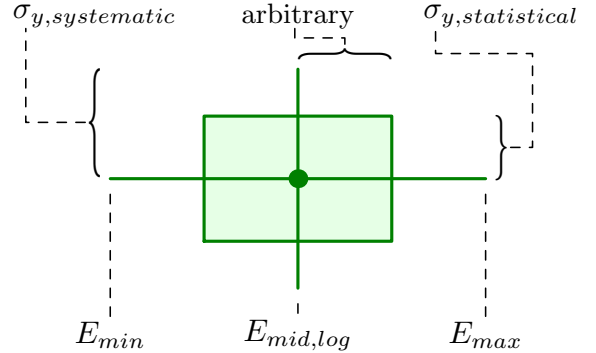

Figure 10: Explanation of each plotted energy bin [18].

4.1. Validation of the deconvolution methodology

The design of the experiment allows for a method to check the performance and accuracy of the deconvolution methodology. While the neutrons from the downstream secondary target were characterized using this methodology out of necessity, it can also be applied to the neutrons produced in the upstream primary target. The upstream neutron energy spectra were previously characterized using time-of-flight techniques [4]. Because pulse height spectra were collected in every measurement, the deconvolution method can be applied to the pulse heights corresponding to neutrons coming directly from the upstream target to generate an energy spectrum. If these two independent and fundamentally different methodologies produce spectra in agreement with each other, the deconvolution methodology can be regarded as trustworthy.

The analysis steps required to characterize the upstream target neutrons through deconvolution only differ from those for the downstream target in two ways. First, rather than using pulse height spectra generated when each detector was concealed with a shadow bar, background subtracted pulse height spectra (shadowed spectra subtracted from unshadowed spectra, after normalization) are used instead. Second, to make the deconvoluted results comparable to the time-of-flight results, they undergo the same solid angle normalization as was done for the upstream target results; this necessitates adding a solid angle component to the total systematic uncertainty [4]. Because the response matrix used in deconvolution only had neutron energies up to 150 MeV, the deconvoluted spectra are also truncated at 150 MeV, an energy that is often exceeded by neutrons produced in the upstream target and detected at the forward angle detectors.

Figure 11 shows the spectra from 400 MeV/n C incident upon the 20 g/cm² Al upstream target at 60° and 80° derived by the two different methods. Note that for the time-of-flight results the width of the shaded boxes is the energy resolution uncertainty and each point is located at a yield-weighted average midpoint.

(a) 60°

(b) 80°
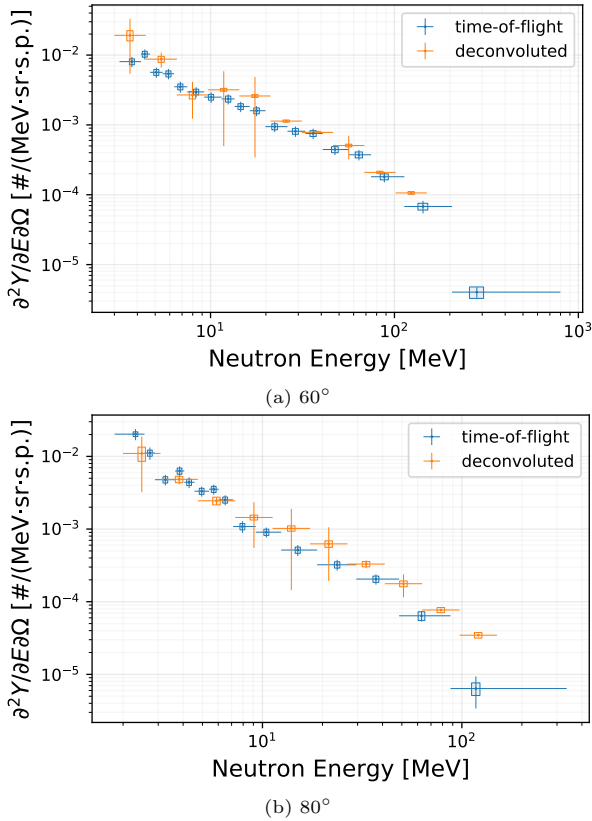
Figure 11: Comparison of time-of-flight and deconvolution methods for neutrons detected at 60° and 80° for 400 MeV/n C incident on the 20 g/cm² Al upstream target.

The two methodologies are in strong agreement with one another here, demonstrating the validity of the deconvolution methodology when applied to neutrons whose energies are largely contained within the response matrix. Figure 12 shows the spectra in the 10° detector derived from both methodologies where a significant fraction of incident neutrons have energies above the response matrix's 150 MeV upper limit.
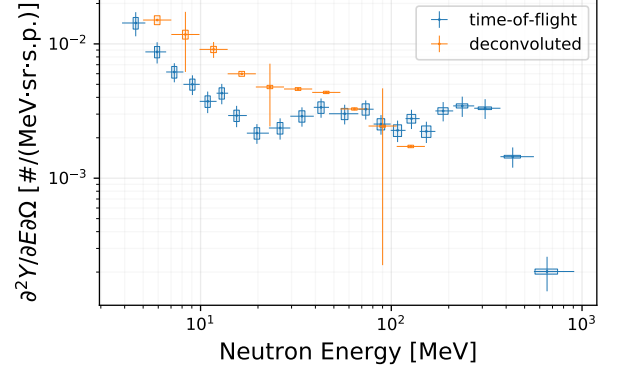

Figure 12: Comparison of time-of-flight and deconvolution methods for neutrons detected at 10° for 400 MeV/n C incident on the 20 g/cm² Al upstream target.

In this case, the yield values from the two methods are fairly close to each other, but the deconvoluted results notably over predict the time-of-flight results at lower energies. This is a common trend when comparing spectra for the two methods for neutrons in the 10° detector where a considerable amount of the upstream target neutron yield spectrum is beyond the 150 MeV limit of the response matrix used in deconvolution. It appears that the additional yield which cannot be attributed to higher energy neutrons is redistributed to lower energy neutrons. This same trend, to a slightly lesser extent, is seen in the 30° (Figure 13) and 45° detectors where a moderate amount of neutron yield is still present above 150 MeV.
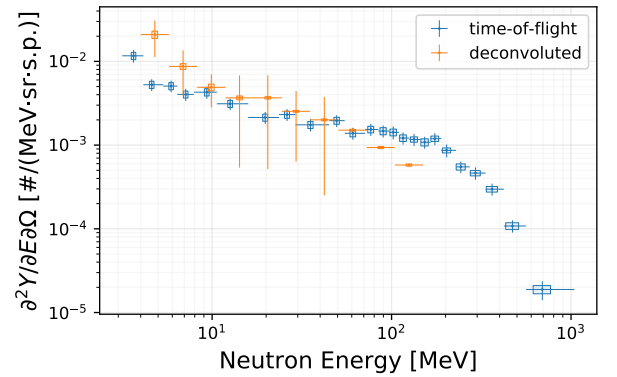

Figure 13: Comparison of time-of-flight and deconvolution methods for neutrons detected at 30° for 400 MeV/n C incident on the 20 g/cm² Al upstream target.

As noted in this example, the differences between the spectra resulting from the two methods subside with increasing detector angle. Additional plots for all six detectors for various example beam/target systems are shown in Appendix B, providing further evidence that these two

methodologies are in agreement when the most abundant neutron energies are almost completely contained in the response matrix.

The neutrons produced in the downstream target (and elsewhere) which are to be characterized using the deconvolution methodology are expected to have energies less than 150 MeV. The reasoning behind this expectation is that the production of neutrons in this experiment can be described using the abrasion-ablation model wherein a projectile nucleus in motion strikes a stationary target nucleus, resulting in three excited fragments: a still-stationary target fragment, a projectile fragment moving at or near the incoming projectile's velocity, and an intermediate rapidity source term (or "fireball") formed from the overlap region of the target and projectile and still in motion (but with lower velocity than the projectile) [19, 20]. These three fragments then de-excite by evaporating nucleons (and clusters). The evaporation is an isotropic process within the reference frame of the source, with emitted particle kinetic energies in that reference frame on the order of several to tens of MeV. When coupled with the velocity of the source, the final trajectory of each evaporated nucleon is determined by the fragment from which it was spawned [21].

Since all of the detectors were located upstream of the secondary target, the vast majority of neutrons detected when the shadow bar was in place were produced either by evaporation of target fragment nuclei in the secondary target or through high angle scattering of projectile and target fragment-produced neutrons. The energies of those neutrons should dominantly fall below 150 MeV, within the bounds of the response matrix, which provides additional confidence that the deconvolution methodology will work for its intended usage: characterization of the downstream target-produced neutrons. The upstream target neutron spectra at higher detector angles, which the deconvolution methodology accurately replicated, are increasingly dominated by target fragment evaporation (as opposed to projectile fragment evaporation) as well.

4.2. Overview of systematic trends

The production of neutrons detected from the secondary target is primarily from neutron scattering and evaporation of target fragment nuclei, both well-known processes, but predicting the magnitudes of the neutron yields from each projectile and target combination is more complex. Neutrons and secondary fragments can be created anywhere in the experiment room, though most abundantly along the beamline. The neutrons from the upstream primary target come exclusively from reactions occurring in the primary target; however, neutrons produced in the downstream secondary target and scattered throughout the room, henceforth referred to as "shadowed neutrons," are influenced by all possible reaction locations.

The most significant neutron production locations are the two thick targets located along the beamline. The largest influencing factor on shadowed neutron yield, aside

from proximity to the secondary target, is beam and secondary fragment penetrability through the upstream target. The beam's stopping location for every combination of projectile and target is shown in Table 3, generated with calculations using the Bethe formula for stopping power [22], where UST denotes the beam stopping in the upstream target, DST denotes the beam penetrating the upstream target but stopping in the downstream target, and DMP denotes the beam penetrating both targets and stopping in the beam dump further downstream.

The primary upstream target is the first major production location of secondary particles and, depending on the beam and target combination, can be the largest source of secondaries in the room. Any surviving primary beam particles and fast-moving and forward-peaked projectile fragments can penetrate the remainder of the primary target if they possess enough energy and then go on to undergo reactions in the secondary downstream target, producing more neutrons there. Additionally, secondary particles produced in the primary target which escape but are not directly bound for a detector or the secondary target can travel throughout the experiment room, scattering or possibly resulting in additional nuclear reactions, and serve as another source of shadowed neutrons. The relevance of each of these production areas is dependent on the penetrability of the beam in each target configuration. For example, beam particles which stop in the upstream target and whose secondary fragments are likely to do so as well will not result in many neutrons produced in the secondary target since only neutrons and perhaps very fast light-charged secondaries will reach the downstream target.

Because the shadowed neutron yield spectra are not normalized for solid angle, detectors nearest to the source of production will have the largest total integrated yields. Figure 14 shows a representative example system where neutron yield directly scales with each detector's proximity to the secondary target, noting that the $10°$ detector placed closest to the secondary target sees the highest yields. In cases with the very least penetrating beams incident upon the most stopping targets, the influence of room-scattered neutrons around the primary target on the detectors closest to it causes the gaps between these spectra to diminish, though the $10°$ detector still sees the most neutrons in those cases.

Due to the $10°$ detector typically having the best statistics and being most influenced by the secondary target, the trends of the yields on beam and target combinations are investigated with data acquired at that angle. The trends to be discussed are the same for the $30°$ and $45°$ detectors as well.

The relationship between beam mass and shadowed neutron yield is a function of both the beam mass and its penetrability. While heavier projectiles have larger total reaction cross sections than lighter projectiles at the same kinetic energy per nucleon on a given target, thus producing more neutrons, the heavier beams and their secondary
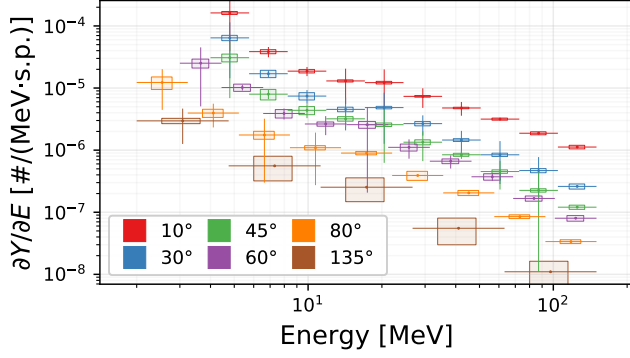
Figure 14: Shadowed neutrons detected at each detector angle from all 800 MeV/n He projectiles incident on the 20 g/cm^2 AlPE upstream target followed by the 60 g/cm^2 HDPE downstream target.
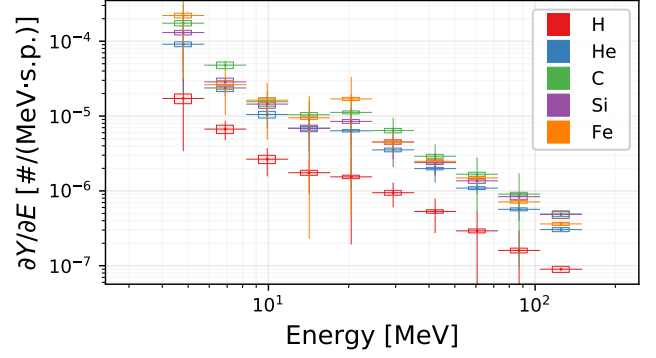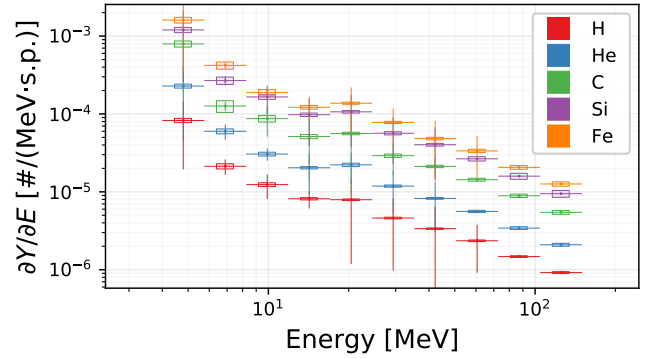

Figure 15: Shadowed neutrons detected at 10° from all 400 MeV/n projectile species incident on the 20 g/cm^2 AlPE upstream target followed by the 60 g/cm^2 HDPE downstream target.

Figure 16: Shadowed neutrons detected at 10° from all 1500 MeV/n projectile species (2500 MeV H) incident on the 20 g/cm^2 AlPE upstream target followed by the 60 g/cm^2 HDPE downstream target.

fragments have, in many cases, insufficient range to penetrate the primary target and reach the secondary target. This interplay of mass and penetrability is highlighted in Figure 15 where 400 MeV/n projectiles of each species were accelerated into the 20 g/cm^2 AlPE hybrid primary target followed by the 60 g/cm^2 HDPE secondary target; in this case, the increased neutron production with increasing mass is roughly counterbalanced by decreased penetrability for the four heaviest projectiles. However, when each species has enough energy to penetrate the primary target, the expected trend of neutron yield scaling with projectile mass is seen, as shown in Figure 16, which shows the same example but with projectiles at 1500 MeV/n instead.

Figures 15 and 16 illustrate that shadowed neutron yield also scales strongly with beam energy since higher beam energies result in more particles (beam ions and sec-

Table 3: Stopping location of all beam projectiles [18]. "UST" = beam stops in upstream target, "DST" = beam penetrates upstream target and stops in downstream target, and "DMP" = beam penetrates both upstream and downstream targets.

Projectile		Upstream target material and thickness (in g/cm^2)							
Species	Energy (MeV/n)	Aluminum			HDPE			Al+HDPE	
		20	40	60	20	40	60	20	60
H	400	DMP	DMP	DST	DST	DST	DST	DST	DST
	800	DMP	DMP	DMP	DMP	DMP	DMP	DMP	DMP
	2500	DMP	DMP	DMP	DMP	DMP	DMP	DMP	DMP
He	400	DMP	DMP	DST	DST	DST	DST	DST	DST
	800	DMP	DMP	DMP	DMP	DMP	DMP	DMP	DMP
	1500	DMP	DMP	DMP	DMP	DMP	DMP	DMP	DMP
C	400	DST	UST	UST	DST	UST	UST	DST	UST
	800	DMP	DST	DST	DST	DST	DST	DST	DST
	1500	DMP	DMP	DMP	DMP	DMP	DMP	DMP	DMP
Si	400	UST	UST	UST	UST	UST	UST	UST	UST
	800	DST	DST	DST	DST	DST	DST	DST	UST
	1500	DMP	DMP	DST	DST	DST	DST	DST	DST
Fe	400	UST	UST	UST	UST	UST	UST	UST	UST
	800	DST	UST	UST	UST	UST	UST	DST	UST
	1500	DST	DST	UST	DST	DST	UST	DST	UST

10

ondary fragments) striking the downstream target, resulting in more secondary neutrons. Figure 17 shows an additional example of this trend with carbon projectiles of each energy incident upon the thinnest and thickest aluminum primary target followed by the 60 g/cm^2 Al secondary target.
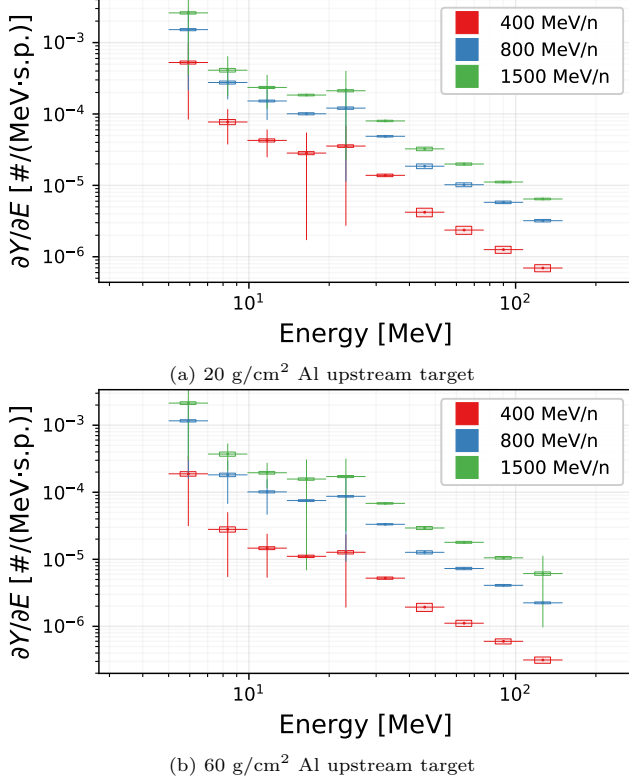

(a) 20 g/cm^2 Al upstream target

(b) 60 g/cm^2 Al upstream target

Figure 17: Shadowed neutrons detected at 10° from C projectiles incident on the 20 g/cm^2 and 60 g/cm^2 Al upstream targets followed by the 60 g/cm^2 Al downstream target.

Clear systematic trends are also present regarding choice of target material. As shown in Figure 18 for 800 MeV/n He projectiles incident upon the extreme thicknesses of each primary target material followed by their respective downstream targets, aluminum targets clearly result in the highest neutron yields while the hybrid AlPE primary targets followed by HDPE secondary targets typically resulted in the lowest neutron yields. The much higher average mass of the target nuclei in aluminum versus polyethylene, thus greater target fragment evaporation source term, and easier penetrability (both for charged particles as well as neutrons) are responsible for why aluminum targets result in the highest neutron yields. However, the explanation for the hybrid AlPE upstream targets resulting in lower yields than the pure HDPE upstream targets of the same mass thicknesses, both followed by the same 60 g/cm^2 HDPE secondary target, is slightly more complicated.

The number of reactions X occurring is proportional to the product of the thickness of material traversed t and macroscopic cross section Σ, where Σ is the product of the

(a) 20 g/cm^2 upstream targets

(b) 60 g/cm^2 upstream targets
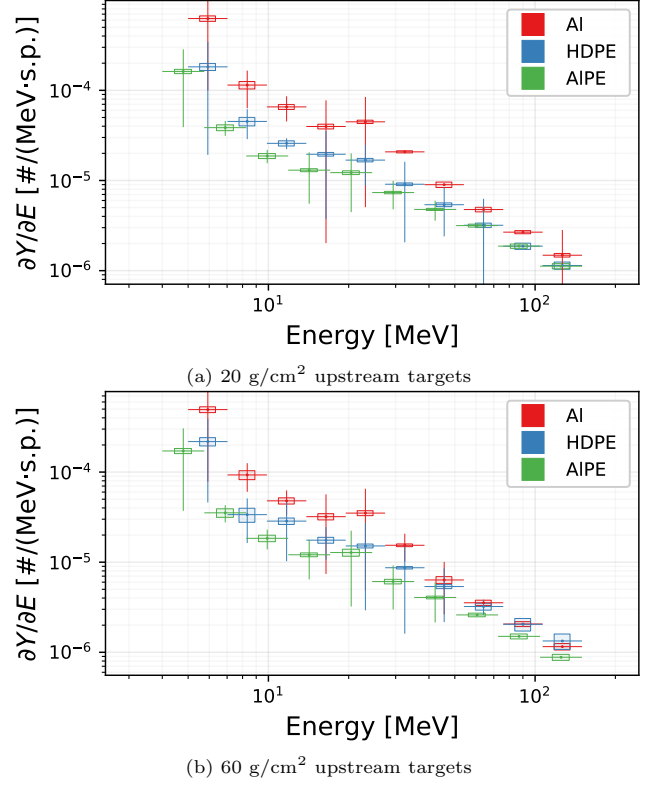
Figure 18: Shadowed neutrons detected at 10° from 800 MeV/n He projectiles incident on the 20 g/cm^2 and 60 g/cm^2 thicknesses of each upstream material composition targets followed by the 60 g/cm^2 downstream target of the same material.

atomic number density N and microscopic cross section σ. The linearity of this proportionality is dependent on the material thickness involved, but it remains that the total number of reactions occurring increases as target thickness increases even after the relationship is no longer approximately linear. Since nuclear collisions are the reactions of concern here, as a simplification σ can be related to the geometric cross section which is proportional to square of the collision radius R. R is the sum of the target and projectile radii which are each proportional to the cube root of the nuclear volumes, which in turn are closely proportional to their masses, A_P and A_T. These proportionalities relating cross section to mass numbers are shown in Equation 6.

$$\Sigma = \sigma N \propto R^2 N \propto \left(A_P^{1/3} + A_T^{1/3} \right)^2 N \qquad (6)$$

The mass thickness, the quantity held constant for each target material, is the product of the thickness t and density ρ of the target material. The density is equal to N times the molar mass $M_{m,T}$ (which is proportional to the target's atomic mass A_T) divided by Avogadro's number A_v. This proportionality is shown in Equation 7.

$$\rho = N M_{m,T}/A_v \propto N A_T \qquad (7)$$

Using Equations 6 and 7, Equation 8 is derived to show how the number of reactions X in a constant mass thick-

ness $t\rho$ of target material trends with the projectile mass A_P and target mass A_T.

$$X \propto \Sigma t = \Sigma \cdot \frac{(t\rho)}{\rho} \propto \left(A_P^{1/3} + A_T^{1/3}\right)^2 N \cdot \frac{(t\rho)}{(NA_T)}$$
$$= (t\rho) \cdot \frac{\left(A_P^{1/3} + A_T^{1/3}\right)^2}{A_T} \qquad (8)$$

The ratios of $X/(t\rho)$, values proportional to the number of reactions per unit mass thickness of material, are shown in Table 4 for the projectiles and target elements of this experiment. From the values given in the table, it is apparent that for a given mass thickness of material that the hydrogenous polyethylene results in more nuclear reactions than aluminum. Thus, one could conclude that the particle flux leaving the primary hybrid targets is less fragmented, and thus has fewer neutrons, than the particle flux leaving a pure HDPE target at the same mass thickness. Due to its high hydrogen content and carbon's lower atomic mass than aluminum, a more significant proportion of the shadowed neutrons detected from the HDPE secondary target are from neutron scattering as opposed to target fragment evaporation (relative to that of the aluminum secondary target). It follows that the incident particle flux with the greater number of neutrons would then result in more neutrons being backscattered toward a detector, thus, accounting for higher shadowed neutron yields from the systems with pure HDPE primary targets relative to those with the hybrid AlPE targets.

Table 4: $X/(t\rho)$ (arbitrary units) for the various projectile/target element combinations.

| Target | Projectile | | | | |
	^{1}H	^{4}He	^{12}C	^{28}Si	^{56}Fe
^{1}H	4.0	6.7	10.8	16.3	23.3
^{12}C	0.9	1.3	1.7	2.4	3.1
^{27}Al	0.6	0.8	1.0	1.3	1.7

While target material choice is typically more impactful on shadowed neutron yield than the primary target's thickness, the significance of primary target thickness is also largely dependent on beam penetrability. The less penetrating the beam is, the more significant the role of upstream target thickness is on the total shadowed neutron yield. Figure 19 shows two systems near opposite extremes of beam penetrability where the yields from the completely penetrating 1500 MeV/n He beam are primarily dependent on material, whereas the yields from the 400 MeV/n Si beam (which is stopped by all upstream targets) are dependent on both target material and thickness.

5. Conclusions

The development and implementation of a deconvolution methodology was presented for characterizing the

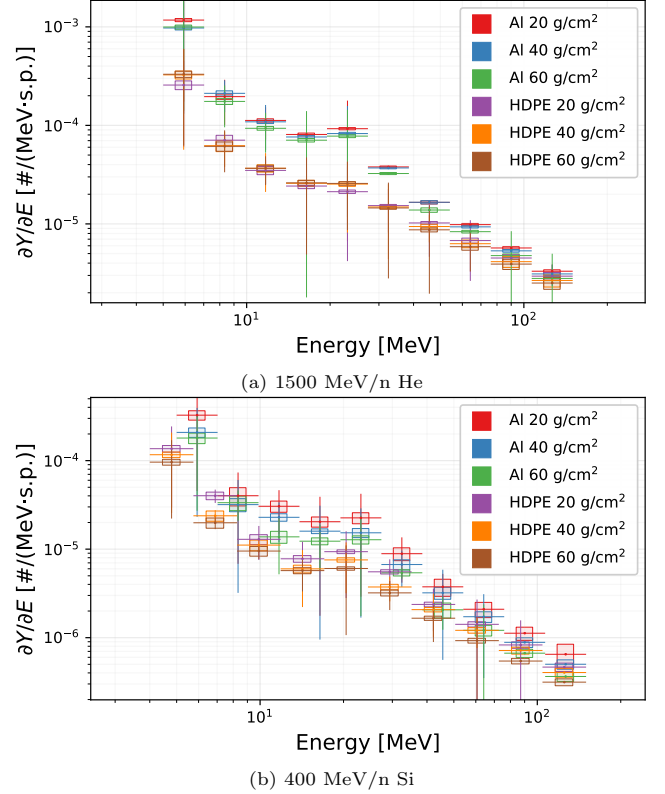(a) 1500 MeV/n He

(b) 400 MeV/n Si

Figure 19: Shadowed neutrons detected at 10° from 1500 MeV/n He and 400 MeV/n Si projectiles incident on the three thicknesses of each pure upstream target material followed by the 60 g/cm^2 downstream target of the same material.

neutrons produced in the secondary target of a dual-target experiment which could not be characterized using standard time-of-flight techniques. The deconvolution process involved Tikhonov regularization followed by L-curve analysis with curvature calculations to determine the optimal level of regularization in a scalable and automated fashion. This methodology relied on response matrices generated with the SCINFUL-QMD code for the organic liquid scintillators used in the experiment along with the measured pulse height spectra to be converted to neutron energy spectra.

To validate the deconvolution methodology, it was also applied to neutrons produced in the primary target which were previously analyzed with time-of-flight techniques. Comparing the two upstream target neutron yields derived from the time-of-flight and deconvolution methodologies proved that the deconvolution methodology produced accurate results as long as the spectra to be characterized were almost completely contained in the energy range of the response matrix used. Due to the physics involved in the production and traversal of neutrons reaching the detectors being concealed by shadow bars, the energies of those neutrons were contained within the response matrix, validating usage of the deconvolution methodology.

A benchmark dataset of secondary target-produced and room-scattered neutron yield spectra was formed. Due to

not having a well-defined production point though, these results could not be normalized to solid angle. Shadowed neutron yields scaled with proximity to the secondary target and beam energy. For very penetrating beams, neutron yields also scaled with projectile mass, and, for not very penetrating beams, neutron yields notably scaled inversely with the primary target's thickness. Aluminum targets resulted in the highest neutron yields, and the hybrid Al+HDPE primary targets followed by pure HDPE secondary targets resulted in the lowest secondary neutron yields. This could serve as a preliminary hint that, for spacecraft shielding applications, configurations resembling the hybrid targets of this experiment could better minimize neutron radiation risk to astronauts than pure aluminum or polyethylene shields.

The repository containing all of the experimental results will be made available from the University of Tennessee's TRACE repository and is also available per request to the author. Additionally, an online tool developed by the author, called SHAEDIT [23], is available at https://github.com/Lindt8/SHAEDIT and can be used for plotting any of the experimental data; this utility was used to generate all of the plots presented in Section 4 of this work.

CRediT authorship contribution statement

Hunter N. Ratliff: Conceptualization, Methodology, Software, Formal analysis, Investigation, Data Curation, Writing - Original Draft, Visualization. **Natalie A. Mc-Girl:** Conceptualization, Methodology, Software, Formal analysis, Investigation. **Matthew R. Beach:** Software, Investigation, Data Curation. **Luis A. Castellanos:** Software, Investigation, Data Curation. **Martha S. Clowdsley:** Investigation, Supervision, Project administration, Funding acquisition. **Lawrence H. Heilbronn:** Conceptualization, Investigation, Resources, Writing - Review & Editing, Supervision, Project administration, Funding acquisition. **Chiara LaTessa:** Conceptualization, Investigation. **John W. Norbury:** Conceptualization, Supervision. **Adam Rusek:** Conceptualization, Investigation, Resources. **Michael Sivertz:** Conceptualization, Investigation, Resources. **Ashwin P. Srikrishna:** Investigation. **Hui-Chen Wang:** Investigation. **Cary Zeitlin:** Conceptualization, Investigation, Writing - Review & Editing, Supervision, Project administration, Funding acquisition.

Acknowledgments

References

[1] T. C. Slaba, A. A. Bahadori, B. D. Reddell, R. C. Singleterry, M. S. Clowdsley, S. R. Blattnig, Optimal shielding thickness for galactic cosmic ray environments, Life Sciences in Space Research 12 (2017) 1–15. doi:10.1016/j.lssr.2016.12.003.

[2] L. Sihver, D. Mancusi, K. Niita, T. Sato, L. Townsend, C. Farmer, L. Pinsky, A. Ferrari, F. Cerutti, I. Gomes, Benchmarking of calculated projectile fragmentation cross-sections using the 3-D, MC codes PHITS, FLUKA, HETC-HEDS, MC-NPX_HI, and NUCFRG2, Acta Astronautica 63 (7) (2008) 865–877. doi:10.1016/j.actaastro.2008.02.012.

[3] J. H. Heinbockel, T. C. Slaba, R. K. Tripathi, S. R. Blattnig, J. W. Norbury, F. F. Badavi, L. W. Townsend, T. Handler, T. A. Gabriel, L. S. Pinsky, B. Reddell, A. R. Aumann, Comparison of the transport codes HZETRN, HETC and FLUKA for galactic cosmic rays, Advances in Space Research 47 (6) (2011) 1089–1105. doi:10.1016/j.asr.2010.11.013.

[4] H. N. Ratliff, N. A. McGirl, M. R. Beach, L. A. Castellanos, M. S. Clowdsley, L. H. Heilbronn, C. LaTessa, J. W. Norbury, A. Rusek, M. Sivertz, A. P. Srikrishna, H.-C. Wang, C. Zeitlin, Double-differential primary target neutron yields from dual-thick-target proton and heavy ion accelerator experiments, Nucl. Instrum. Methods Phys. Res., B, *submitted concurrently*.

[5] L. H. Heilbronn, C. Zeitlin, M. R. Beach, L. A. Castellanos, M. S. Clowdsley, C. LaTessa, N. A. McGirl, J. W. Norbury, H. N. Ratliff, A. Rusek, M. Sivertz, A. P. Srikrishna, H.-C. Wang, Design of an accelerator-based experiment relevant to enclosed, shielded environments in space, Nucl. Instrum. Methods Phys. Res., B, *submitted concurrently*.

[6] C. C. Lawrence, Neutron spectrum unfolding with organic scintillators for arms-control verification, Ph.D. thesis, The University of Michigan (2014).

[7] M. Sasaki, N. Nakao, T. Nakamura, T. Shibata, A. Fukumura, Measurements of the response functions of an NE213 organic liquid scintillator to neutrons up to 800 MeV, Nucl. Instrum. Methods Phys. Res., A 480 (2–3) (2002) 440–447. doi:10.1016/S0168-9002(01)00948-2.

[8] D. Satoh, S. Kunieda, Y. Iwamoto, N. Shigyo, K. Ishibashi, Development of SCINFUL-QMD code to calculate the neutron detection efficiencies for liquid organic scintillator up to 3 GeV, Journal of Nuclear Science and Technology 39 (sup2) (2002) 657–660. doi:10.1080/00223131.2002.10875185.

[9] J. K. Dickens, SCINFUL: A Monte Carlo based computer program to determine a scintillator full energy response to neutron detection for E_n between 0.1 and 80 MeV: Program development and comparisons of program predictions with experimental data, Tech. rep., Oak Ridge National Laboratory (1988). doi:10.2172/7166672.

[10] N. Nakao, T. Kurosawa, T. Nakamura, Y. Uwamino, Absolute measurements of the response function of an NE213 organic liquid scintillator for the neutron energy range up to 206 MeV, Nucl. Instrum. Methods Phys. Res., A 463 (1–2) (2001) 275–287. doi:10.1016/S0168-9002(01)00260-1.

[11] D. Satoh, T. Sato, A. Endo, Y. Yamaguchi, M. Takada, K. Ishibashi, Measurement of Response Functions of a Liquid Organic Scintillator for Neutrons up to 800 MeV, Journal of Nuclear Science and Technology 43 (2006) 714–719. doi:10.1080/18811248.2006.9711153.

[12] J. F. Ziegler, M. D. Ziegler, J. P. Biersack, Srim – the stopping and range of ions in matter (2010), Nucl. Instrum. Methods Phys. Res., B 268 (11) (2010) 1818–1823, 19th International Conference on Ion Beam Analysis. doi:10.1016/j.nimb.2010.02.091.

[13] P. Žugec, N. Colonna, M. Sabate-Gilarte, V. Vlachoudis, C. Massimi, J. Lerendegui-Marco, A. Stamatopoulos, M. Bacak, S. G. Warren, A direct method for unfolding the resolution function from measurements of neutron induced reactions, Nucl. Instrum. Methods Phys. Res., A 875 (2017) 41–50. doi:10.1016/j.nima.2017.09.004.

[14] D. Calvetti, S. Morigi, L. Reichel, F. Sgallari, Tikhonov regularization and the L-curve for large discrete ill-posed problems, Journal of Computational and Applied Mathematics 123 (1–2) (2000) 423–446, Numerical Analysis 2000. Vol. III: Linear Algebra. doi:10.1016/S0377-0427(00)00414-3.

[15] P. C. Hansen, The L-Curve and its use in the numerical treatment of inverse problems, in: Computational Inverse Problems in Electrocardiology, ed. P. Johnston, Advances in Computational Bioengineering, WIT Press, 2000, pp. 119–142.

[16] P.-E. Tsai, Study of secondary particles produced from heavy-ion interactions, Ph.D. thesis, The University of Tennessee, Knoxville (2015).

[17] T. Nakamura, L. Heilbronn, Handbook on Secondary Particle Production and Transport by High-energy Heavy Ions:(with CD-ROM), World Scientific, 2006. doi:10.1142/5973.

[18] H. N. Ratliff, Thick-target neutron yields for intermediate-energy heavy ion experiments at NSRL, Ph.D. thesis, The University of Tennessee, Knoxville (2018).

[19] L. W. Townsend, J. W. Wilson, J. W. Norbury, H. B. Bidasaria, An abrasion-ablation model description of galactic heavy-ion fragmentation, NASA technical paper, National Aeronautics and Space Administration, Scientific and Technical Information Branch, 1984.
URL https://ntrs.nasa.gov/citations/19840014328

[20] F. A. Cucinotta, J. W. Wilson, L. W. Townsend, Abrasion-ablation model for neutron production in heavy ion collisions, Nuclear Physics A 619 (1) (1997) 202–212. doi:10.1016/S0375-9474(97)00130-9.

[21] J. Gosset, H. H. Gutbrod, W. G. Meyer, A. M. Poskanzer, A. Sandoval, R. Stock, G. D. Westfall, Central collisions of relativistic heavy ions, Phys. Rev. C 16 (1977) 629–657. doi:10.1103/PhysRevC.16.629.

[22] J. E. Turner, Atoms, Radiation, and Radiation Protection, Wiley, 2008. doi:10.1002/9783527616978.

[23] H. N. Ratliff, SHAEDIT: Space Hadron Accelerator Experiment Data Investigation Tool (2018). doi:10.5281/zenodo.1291203.
URL https://github.com/Lindt8/SHAEDIT

[24] R. A. Johnson, Modern Geometry: An Elementary Treatise on the Geometry of the Triangle and the Circle, Houghton, Mifflin company, 1929.
URL http://hdl.handle.net/2027/wu.89043163211

[25] M. Kline, Calculus: An Intuitive and Physical Approach, Dover Books on Mathematics, Dover Publications, 1998.

Appendix A. Formation of the curvature equation

A circle can be fit to any three distinct and non-collinear Cartesian points F, G, and H with coordinates of (x_1, y_1), (x_2, y_2), and (x_3, y_3), respectively. Non-collinearity can be proven in a variety of ways, though proving that the triangle formed by these three points (Figure A.1) has nonzero area is convenient here since the area will be a useful quantity later.
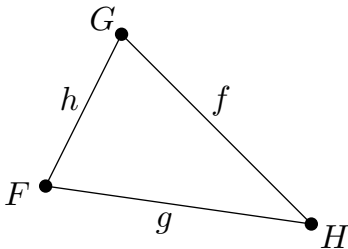

Figure A.1: Triangle formed by triplet of points to be fit with a circle.

The Shoelace formula (also known as Gauss's area formula) can be employed for the $n = 3$ case (where n is the polygon's number of sides) to find the area of the triangle as shown in Equation A.1; note that x_{n+1} and y_{n+1} are equal to x_1 and y_1, respectively. This result can be negative depending on the ordering of the points, so the absolute value in the last step has been added to prevent this.

$$
\begin{aligned}
A &= \frac{1}{2} \sum_{i=1}^{3} \begin{vmatrix} x_i & x_{i+1} \\ y_i & y_{i+1} \end{vmatrix} \\
&= \frac{1}{2} \left(\begin{vmatrix} x_1 & x_2 \\ y_1 & y_2 \end{vmatrix} + \begin{vmatrix} x_2 & x_3 \\ y_2 & y_3 \end{vmatrix} + \begin{vmatrix} x_3 & x_1 \\ y_3 & y_1 \end{vmatrix} \right) \\
&= \frac{1}{2} (x_1 y_2 - x_2 y_1 + x_2 y_3 - x_3 y_2 + x_3 y_1 - x_1 y_3) \\
|A| &= \frac{1}{2} |(x_2 - x_1) \cdot (y_3 - y_2)) - ((y_2 - y_1) \cdot (x_3 - x_2)|
\end{aligned}
\tag{A.1}
$$

The side lengths opposite the vertices F, G, and H will be denoted by the same letters in lowercase: f, g, and h, respectively. The circle's radius R can be found using Equation A.2 [24, pg.11].

$$
R = \frac{fgh}{4A}
\tag{A.2}
$$

These side lengths can be calculated using the Cartesian distance formula (Table A.5) and then inserted back into Equation A.2 alongside the triangle's area from Equation A.1 to obtain the radius R in terms of only the original three points' coordinates as shown in Equation A.3.

Table A.5: Triangle side lengths.

| Segment	Name	Length
$\overline{FG}$	h	$\sqrt{(x_2 - x_1)^2 + (y_2 - y_1)^2}$
$\overline{GH}$	f	$\sqrt{(x_3 - x_2)^2 + (y_3 - y_2)^2}$
$\overline{HF}$	g	$\sqrt{(x_1 - x_3)^2 + (y_1 - y_3)^2}$

$$
R = \frac{\left([(x_2 - x_1)^2 + (y_2 - y_1)^2] \cdot [(x_3 - x_2)^2 + (y_3 - y_2)^2] \cdot [(x_1 - x_3)^2 + (y_1 - y_3)^2] \right)^{1/2}}{2 \cdot |((x_2 - x_1) \cdot (y_3 - y_2)) - ((y_2 - y_1) \cdot (x_3 - x_2))|}
\tag{A.3}
$$

The curvature κ of three points is simply the inverse of this radius and is shown in Equation A.4 [25, pp.457,458]. Note that the absolute value in the numerator can be removed if differentiating between negative and positive curvature is desired.

$$\kappa = \frac{1}{R} = \frac{4A}{fgh}$$

$$= \frac{2 \cdot |((x_2 - x_1) \cdot (y_3 - y_2)) - ((y_2 - y_1) \cdot (x_3 - x_2))|}{\begin{array}{c}([[(x_2 - x_1)^2 + (y_2 - y_1)^2] \\ \cdot [(x_3 - x_2)^2 + (y_3 - y_2)^2] \\ \cdot [(x_1 - x_3)^2 + (y_1 - y_3)^2])^{1/2}\end{array}}$$

<div align="right">(A.4)</div>

## Appendix B. Additional comparison of time-of-flight and deconvolution-derived neutron spectra

Supplemental comparisons of results derived from the time-of-flight and deconvolution methodologies for neutrons produced in the upstream target are shown here. Plots for all six detectors are shown for 1500 MeV/n He incident upon the 60 g/cm^2 Al upstream target in Figure B.1, for 400 MeV H incident upon the 20 g/cm^2 Al upstream target in Figure B.2, and for 400 MeV/n Si incident upon the 20 g/cm^2 HDPE upstream target in Figure B.3.

(a) 10°

(b) 30°

(c) 45°
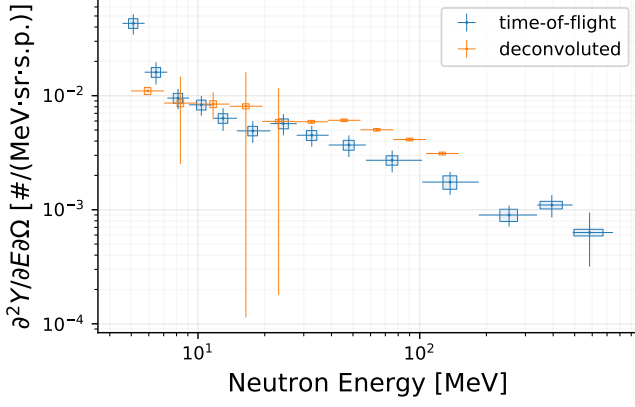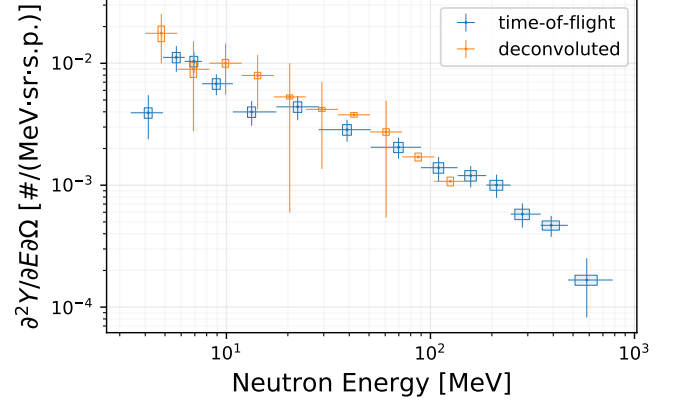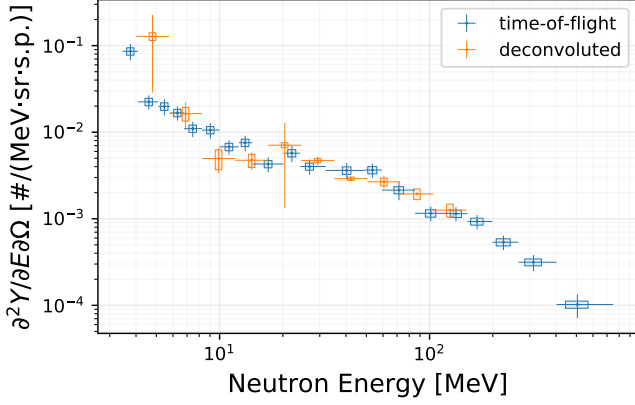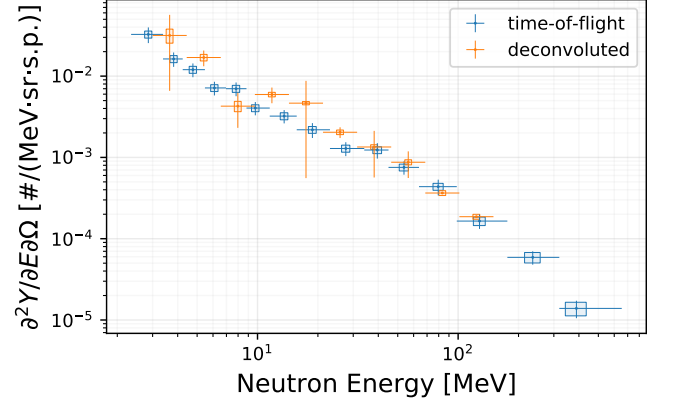
(d) 60°
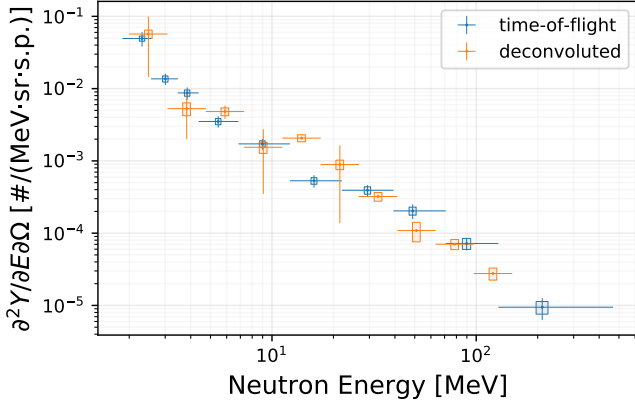
(e) 80°
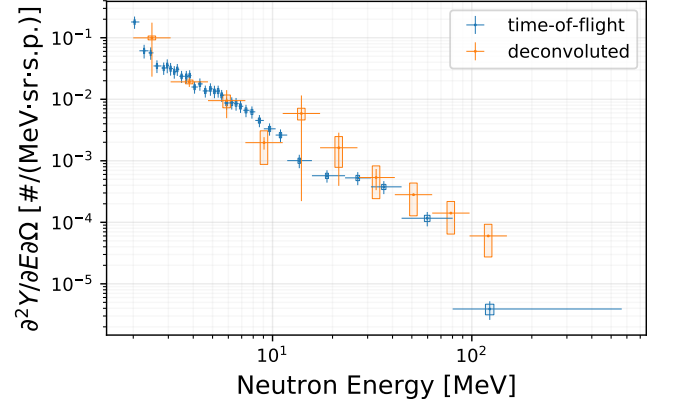
(f) 135°

Figure B.1: Comparison of time-of-flight and deconvolution methods for neutrons detected at all angles for 1500 MeV/n He incident on the 60 g/cm² Al upstream target.
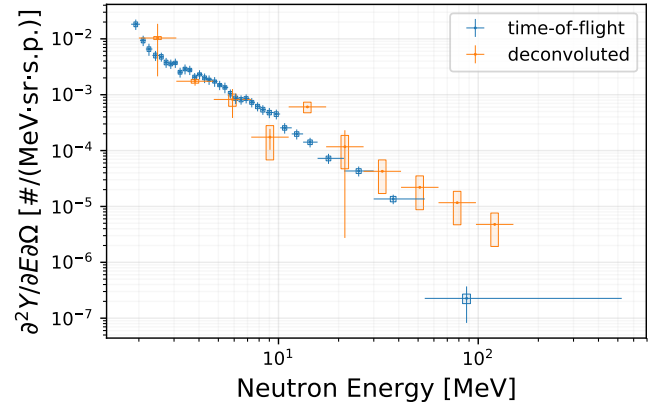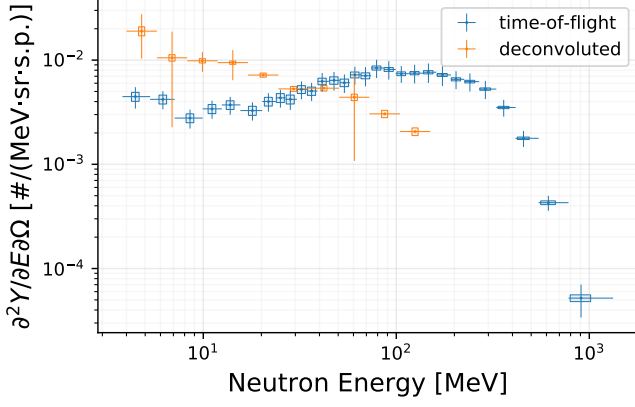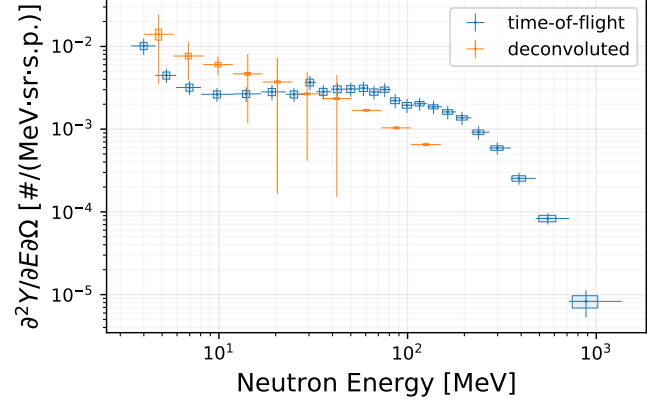
(a) 10°

(b) 30°

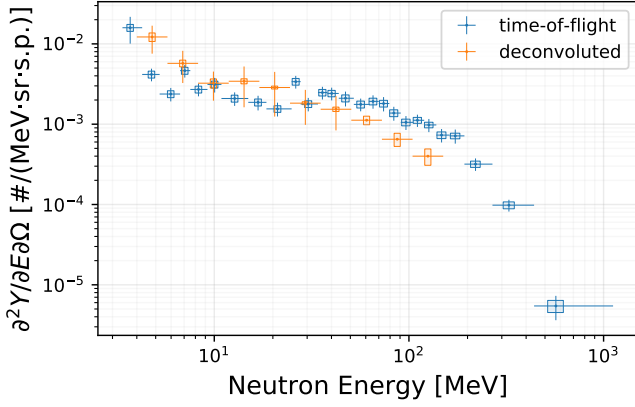(c) 45°
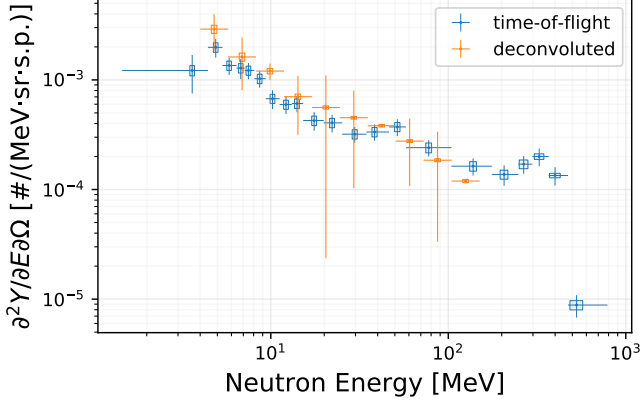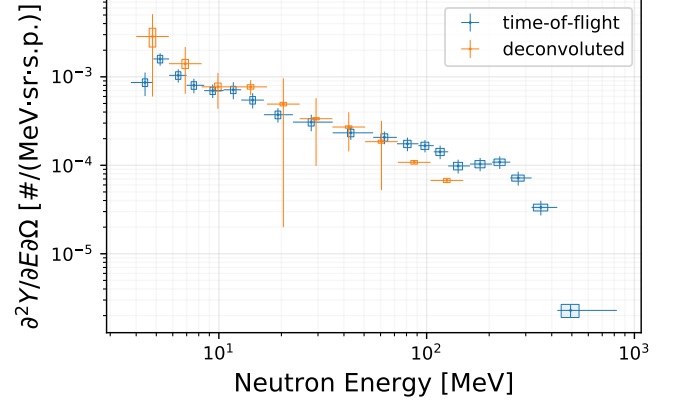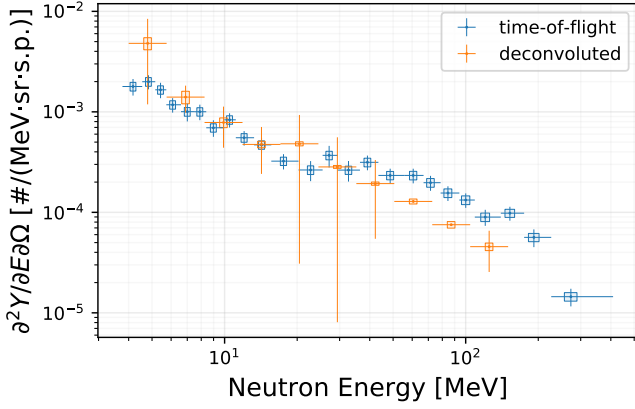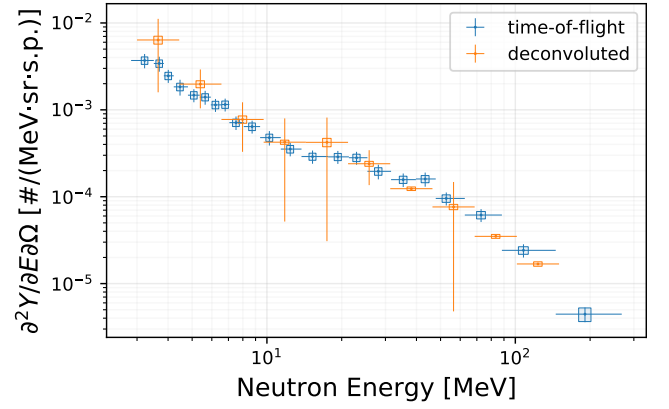
(d) 60°
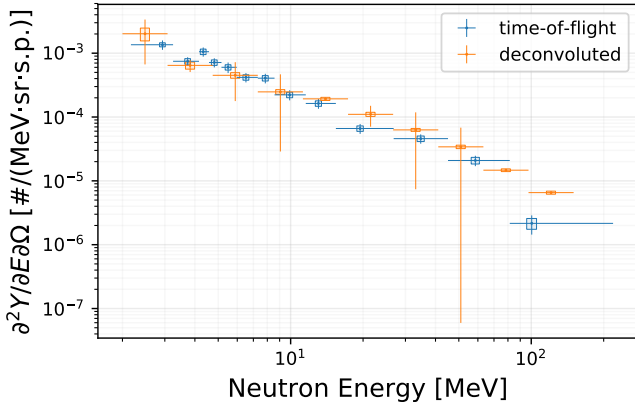
(e) 80°

(f) 135°

Figure B.2: Comparison of time-of-flight and deconvolution methods for neutrons detected at all angles for 400 MeV H incident on the 20 g/cm² Al upstream target.
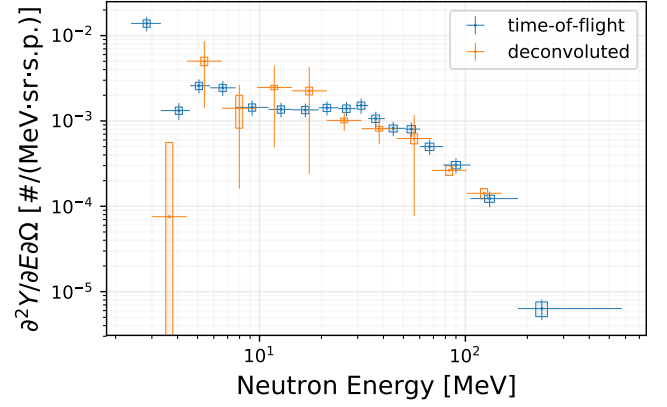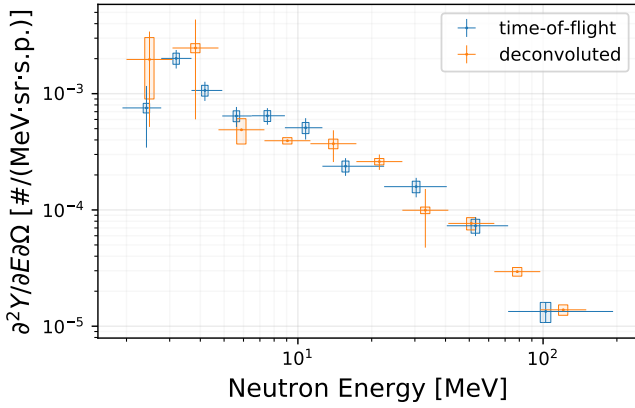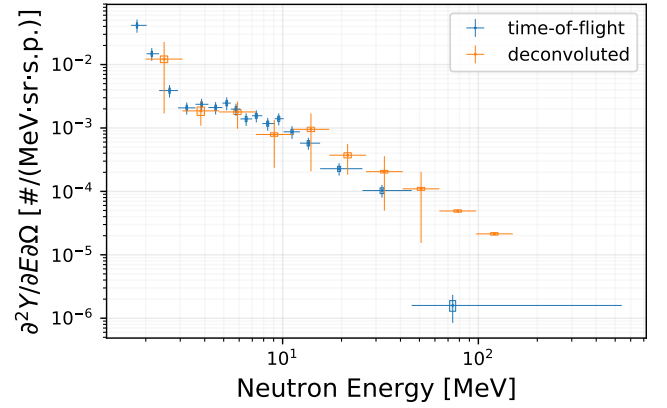
(a) 10°

(b) 30°

(c) 45°

(d) 60°

(e) 80°

(f) 135°

Figure B.3: Comparison of time-of-flight and deconvolution methods for neutrons detected at all angles for 400 MeV/n Si incident on the 20 g/cm^2 HDPE upstream target.